SCIENTIFIC REPORTS

OPEN

SUBJECT AREAS:
BIOPHYSICS
BIOMARKERS
BIOMEDICAL ENGINEERING
IMAGING TECHNIQUES

Received
13 May 2013

Accepted
27 August 2013

Published
12 September 2013

Correspondence and requests for materials should be addressed to X.-C.Y. (xcy@uab.edu)

In vivo Optical Coherence Tomography of Light-Driven Melanosome Translocation in Retinal Pigment Epithelium

Qiu-Xiang Zhang[1], Rong-Wen Lu[1], Jeffrey D. Messinger[2], Christine A. Curcio[2], Vincenzo Guarcello[3] & Xin-Cheng Yao[1,3,4]

[1]Department of Biomedical Engineering, University of Alabama at Birmingham, Birmingham, AL 35294, [2]Department of Ophthalmology, University of Alabama at Birmingham, Birmingham, AL 35294, [3]Vision Science Research Center, University of Alabama at Birmingham, Birmingham, AL 35294, [4]Department of Vision Sciences, University of Alabama at Birmingham, Birmingham, AL 35294.

Optical coherence tomography (OCT) may revolutionize fundamental investigation and clinical management of age-related macular degeneration and other eye diseases. However, quantitative OCT interpretation is hampered due to uncertain sub-cellular correlates of reflectivity in the retinal pigment epithelium (RPE) and photoreceptor. The purpose of this study was twofold: 1) to test OCT correlates in the RPE, and 2) to demonstrate the feasibility of longitudinal OCT monitoring of sub-cellular RPE dynamics. A high resolution OCT was constructed to achieve dynamic imaging of frog eyes, in which light-driven translocation of RPE melanosomes occurred within the RPE cell body and apical processes. Comparative histological examination of dark- and light-adapted eyes indicated that the RPE melanin granule, i.e., melanosome, was a primary OCT correlate. In vivo OCT imaging of RPE melanosomes opens the opportunity for quantitative assessment of RPE abnormalities associated with disease, and enables longitudinal investigation of RPE kinetics correlated with visual function.

This study was designed to achieve two objectives simultaneously: 1) to investigate optical coherence tomography (OCT) correlates in the retinal pigment epithelium (RPE); 2) to demonstrate the feasibility of in vivo OCT monitoring of RPE dynamics at sub-cellular level. Located posterior to the photoreceptors at the back of the eye, the RPE is a simple cuboidal epithelium attached firmly to the neurosensory retina at the apical aspect and Bruch's membrane at the basal aspect. The RPE is essential in maintaining physiological function of photoreceptors and choroidal vasculature[1,2]. It is known that the RPE plays multiple roles including phagocytosing retinal photoreceptors[3], manufacturing the photopigment 11-cis retinal[4,5], transporting nutrients and new retinoid from choriocapillaris[3], and scavenging stray light[6]. RPE abnormalities can occur in eye diseases, including age-related macular degeneration (AMD)[7,8], which is a leading cause of impaired vision and legal blindness[9,10]. In the U.S. alone, more than 10 million people are estimated to have early AMD, and 1.75 million patients suffer visual impairment due to late AMD[11]. A key to preventing the sight-threatening damages of late AMD is reliable detection and assessment of early AMD. By providing unprecedented resolution to differentiate individual retinal layers, optical coherence tomography (OCT) may revolutionize the fundamental study and clinical management of AMD and other eye diseases[12–18]. However, quantitative interpretation of the OCT outcomes is challenging by uncertain OCT correlates to subcellular structures in RPE and photoreceptors[19,20].

Melanin granules (i.e., melanosomes) are candidate OCT reflectivity sources in the RPE[19,20], but direct evidence has not been provided. In this study, we selected leopard frog for testing the contribution of RPE melanosomes to OCT reflectivity. It is known that light-driven translocation of RPE melanin granules (i.e., melanosomes) can occur in frog eyes[21] and other animal species[22,23]. Based on early histological study[21], it has been established that frog RPE melanosomes could move into the proximal ends of the RPE apical processes (microvilli) in dark-adapted retinas (Fig. 1, left). In contrast, RPE melanosomes migrate distally within the apical processes, which interdigitated with the photoreceptors, in light-adapted retinas (Fig. 1, right). The light-driven translocation of frog RPE melanosomes provided an excellent model to quantify the contribution of RPE melanin to

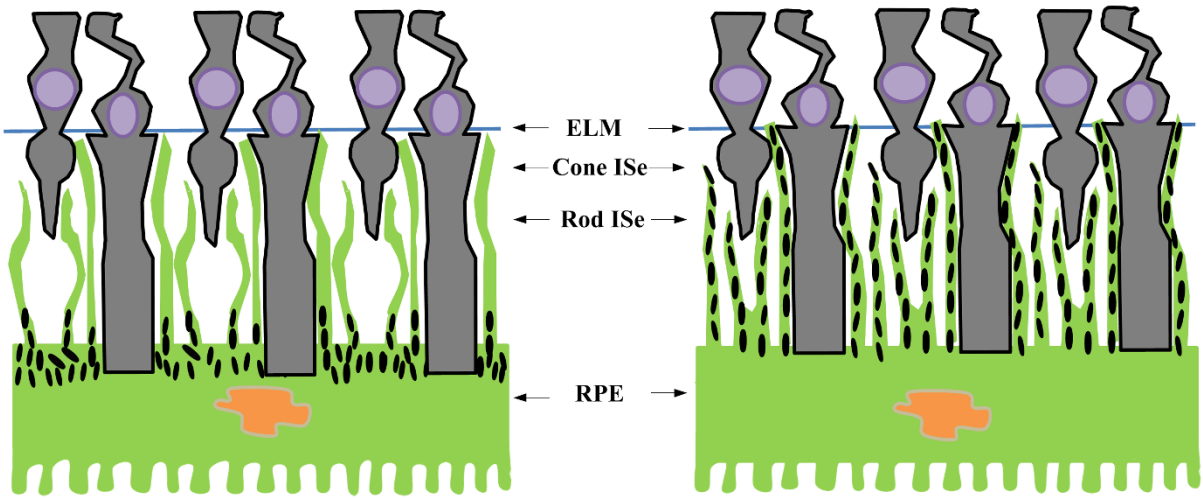

Figure 1 | Cartoon illustration of melanosome position in dark-adapted (left) and light-adapted (right) frog retinas. RPE melanosomes are confined in the basal ends of the RPE cells in dark-adapted retinas; while they migrate into the apical projections in light-adapted retinas. ISe, inner segment ellipsoid.

OCT-detectable reflectivity. If the melanosome is a primary OCT correlate in the RPE, high OCT reflectivity of the RPE band should be expected in dark-adapted retina, due to melanosomes confined in the basal RPE (Fig. 1, left). In contrast, reduced reflectivity of the RPE band and enhanced reflectivity of the photoreceptor and external limiting membrane (ELM) zone should be expected in light-adapted retina, due to melanosome translocation within the apical processes from proximal (near the RPE cell body) to distal (near the ELM) (Fig. 1, right).

We tested the hypothesis by comparing OCT scans of dark- and light-adapted frog retinas. A custom-designed spectral domain OCT (SD-OCT) was developed to provide sub-cellular resolution in both lateral (2 μm) and axial (3 μm) directions. Hyper-reflective OCT bands that encompass the RPE, photoreceptor, and ELM were quantitatively analyzed. Our observed OCT dynamics showed tight correlation with RPE melanosome migration, and the feasibility of dynamic OCT monitoring of sub-cellular RPE translocation was demonstrated for the first time.

Results

OCT imaging of dark-adapted and light-adapted frog eyes. The OCT images in Fig. 2A1–A2 were collected from two different frogs that were dark-adapted over-night. The OCT images in Fig. 2B1–B2 were collected from two different frogs with 8-hour light adaptation. Before each OCT recording, with the reference arm at a stationary position, we adjusted the position of nerve fiber layer located near 150 μm from the zero-depth position (positive delay) first. The position adjustment was based on dynamic monitoring of the reflectivity profile of the twin (real/mirror) OCT A-lines. After that, the reference arm and the sample arm were adjusted simultaneously, i.e., in the same direction and same distance, to focus the light at the photoreceptor layer, where we observed the sharpest pattern of photoreceptor mosaic. Each B-scan image consisted of 512 A-scans. OCT reflectivity profiles averaged over 50 A-scans across whole retinal depth were superimposed on B-scan images in Fig. 2A1 (dashed yellow line), Fig. 2A2 (solid yellow line), Fig. 2B1 (dashed red line) and Fig. 2B2 (solid red line). In dark-adapted eyes, sub-cellular resolution B-scan (i.e. cross-sectional) OCT images consistently revealed a hyper-reflective band at the RPE. The ELM and photoreceptor inner segment ellipsoid (ISe) could be unambiguously differentiated (Fig. 2A1–A2). In comparison with OCT images of dark-adapted eyes (Fig. 2A1–A2), both reflectivity and bandwidth of the RPE band were decreased significantly in light-adapted eyes (Fig. 2B1–B2). Moreover, the ELM and ISe bands were merged together. Therefore, the ISe OCT band in the eye with light adaptation became wider compared to that in the eye with dark adaptation.

In order to verify the axial locations of individual OCT bands, en-face (i.e., projection) images of the retina/RPE were reconstructed (Fig. 2C–D). En face images (projection within 25 μm depth) of the nerve fiber layer (Fig. 2C) and photoreceptor outer segment (OS) (Fig. 2D) were reconstructed from the same data set of 400 B-scans. The display window and level of each enface projection image (Fig. 2C–D) was adjusted separately for a better visualization of cellular structures. In Fig. 2C, individual blood vessels were clearly observed. The photoreceptor mosaic was unambiguously shown in Fig. 2D. By superimposing the reflectivity profiles (from NFL to RPE complex) generated from Fig. 2A1–A2 and Fig. 2B1–B2, significant OCT changes were revealed only at the outer retina/RPE; while the OCT change of inner retina (from NFL to OPL) were negligible (Fig. 2E).

In order to verify the repeatability of the observation, eight dark-adapted and eight light-adapted frogs have been used for comparative OCT imaging. Table 1 illustrates quantified thicknesses of the RPE-ISe layer (blue bars in Fig. 2A–B) and whole retina including the RPE (green bars in Fig. 2A–B) of the sixteen frogs. Statistical analysis revealed significant change of the RPE-ISe layer thicknesses ($p < .00005$, student's t-test) between dark- and light-adapted conditions. In contrast, no significant differences were observed in the retinal thicknesses ($p > 0.5$, student's t-test) between dark- and light-adapted conditions. Box charts with data overlay in Fig. 3. revealed that the thickness of the RPE-ISe layer increased in light-adapted condition compared to that in dark-adapted condition.

OCT imaging of light-to-dark transition in frog eyes. In order to verify the reliability of OCT changes correlated with light conditions, we conducted dynamic OCT imaging of a frog eye over ~1 hour (Fig. 4). The frog was light-adapted for 8 hours, and OCT images were captured continuously during the transition from light to dark at the same retinal location. Fig. 4A shows the cross-sectional image in light condition. After the light was turned off, the frog was maintained in the dark room for longitudinal OCT monitoring. After 1 hour in the dark room, the ELM was gradually appeared as an individual layer in Fig. 4B, which was mixed with the ISe band in Fig. 4A. Fig. 4C–F shows light intensity distribution changes in local cross-sectional images 0 min, 20 min, 40 min and 60 min later after the light-adapted eye was left in the darkness. As we can see, inner retina only changed slightly over time. In contrast, in the outer retina, the peak of reflected light was gradually translated to the outermost layer. Basically, it took as long as 60 min for pigment to transit from light-adapted to dark-adapted position.

Table 1 | Summary of 16 frogs under dark- and light-adapted conditions

Light-adapted			Dark-adapted		
Frog	RPE-ISe thickness (μm)	Retina thickness (μm)	Frog	RPE-ISe thickness (μm)	Retina thickness (μm)
1	75	216	9	70	212
2	76	212	10	74	218
3	75	211	11	68	213
4	74	223	12	67	216
5	77	220	13	68	220
6	79	209	14	73	216
7	78	222	15	68	203
8	77	220	16	70	220

In order to quantify the light reflectivity change, linear scale was used in the images in Fig. 5A. The averaged reflected light changes of outer retina and inner retina were plotted in Fig. 5B. It was observed that the total light reflected from outer retina and inner retina were almost constant (<±7% change over time) during the light-dark transition. The slight difference might reflect the effect of pigment bleaching and outer segment changes correlated with retinal adaptation. Therefore, it further supports our hypothesis that the observed

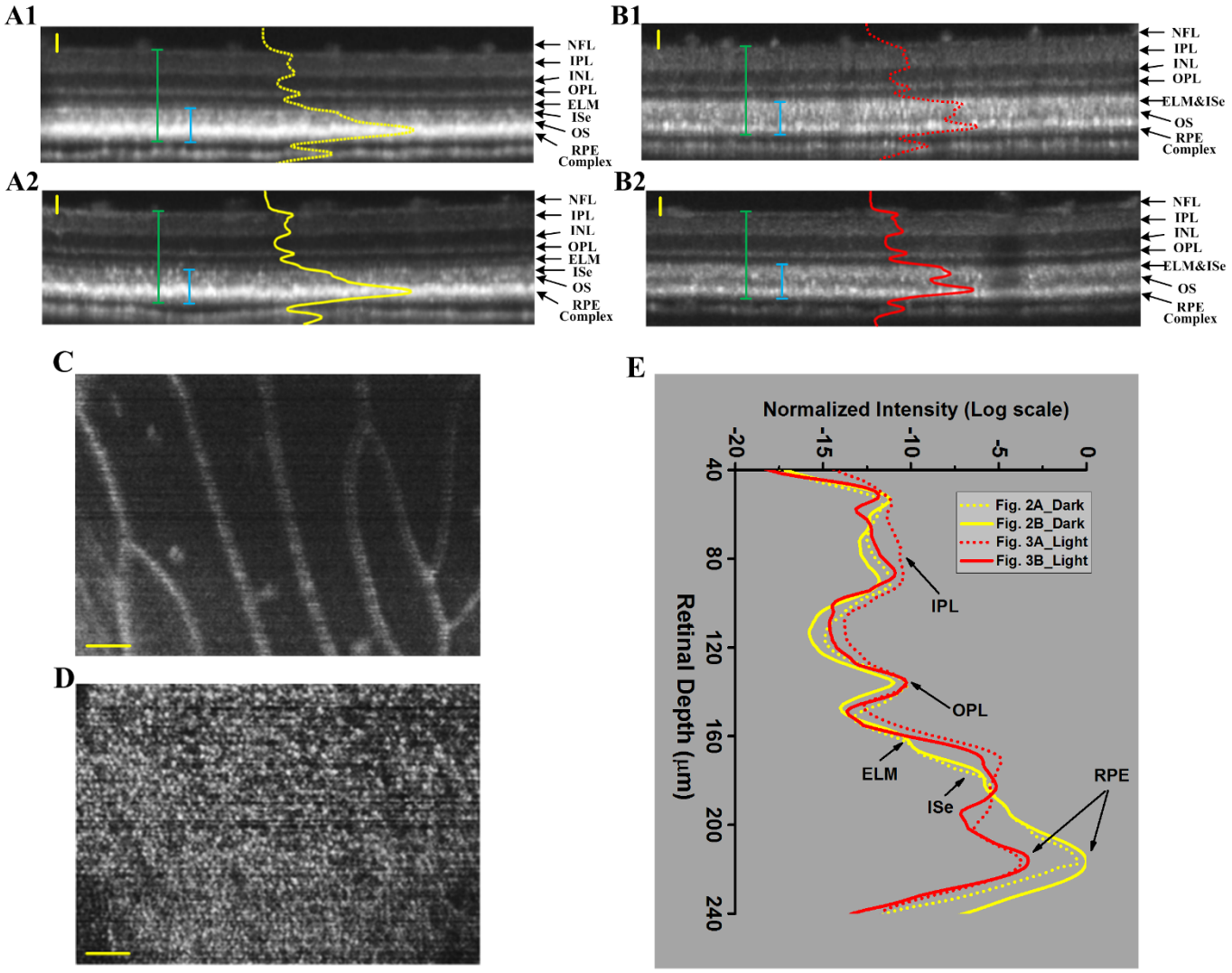

Figure 2 | Representative OCT images of dark-adapted and light-adapted frog eyes. The cross-sectional images (A1) and (A2) were collected from two separate frogs, with over-night dark adaptation. NFL: nerve fiber layer, IPL: inner plexiform layer, INL: inner nuclear layer, OPL: outer plexiform layer, ELM: external limiting membrane, IS: inner segment, OS: outer segment and RPE: retinal pigment epithelium. The cross-sectional images (B1) and (B2) were collected from two separate frogs, with 8-hour light adaptation. The green bars measured the retinal thickness with RPE complex included and the blue bars measured the RPE-ISe layer thickness; (C) Reconstructed en-face projection of blood vessels obtained nearby the NFL layer in Fig. 2A1; (D) Reconstructed en-face projection of photoreceptor mosaic obtained from the photoreceptor layer in Fig. 2A1. The contrast and brightness were adjusted for best visualization. (E) OCT reflectivity profiles of dark- (yellow) and light- (red) adapted frog eyes. The two yellow traces correspond to the two dark-adapted images in Fig. 2A1–2A2. The two red traces correspond to the two light-adapted images in Fig. 2B1–B2. Scale bars indicate 50 μm.

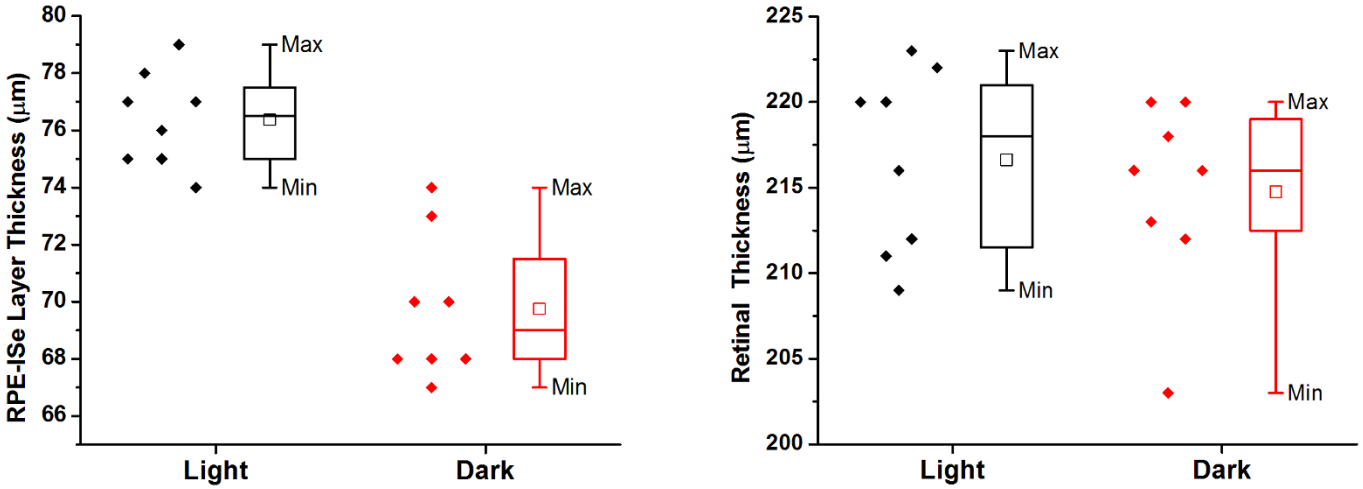

Figure 3 | Box charts show RPE-ISe layer thickness (left) and retinal thickness (right) with data overlay. Box = 25th and 75th percentile.

light changes in outer retina and RPE complex were tightly correlated with light-driven melanosome translocation.

Histological images of dark- and light-adapted frog eyes. In order to verify the light-driven melanosome translocation, histological examination of dark- and light-adapted frog eyes was conducted. Fig. 6A–B shows transmission microscopy (40×) images of 14 μm-thick cryostat sections of eyecup slices with dark (Fig. 6A) and light (Fig. 6B) adaptations, respectively. We speculate that the significant difference at the RPE/photoreceptor attributed to RPE

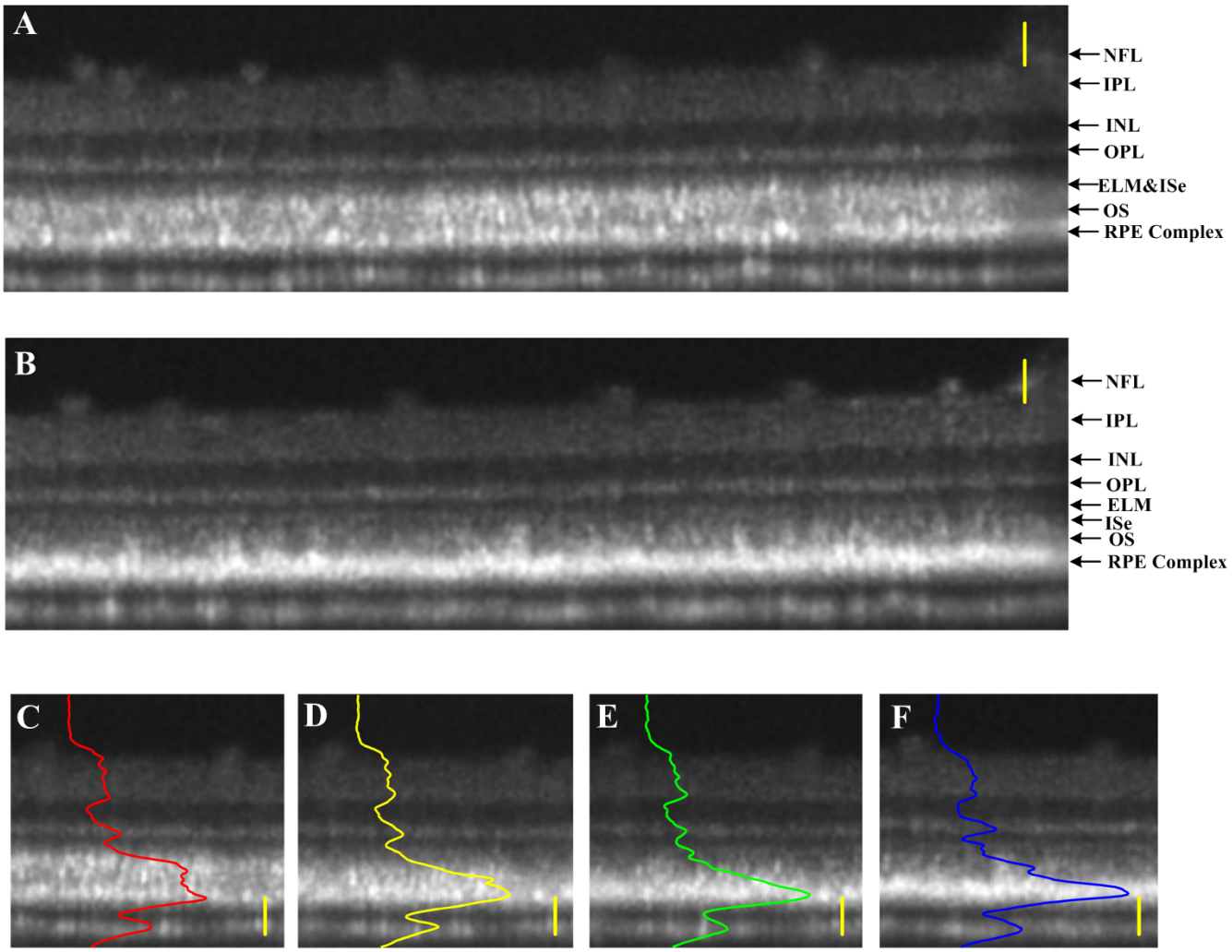

Figure 4 | OCT imaging of retina during light-to-dark transition. (A) Cross-sectional image of light-adapted frog eye; (B) Cross-sectional image at the identical location in the retina 1 hour later after maintained in the darkness. Panels (C–F) illustrate the same local areas of the cross-sectional images recorded at 0-min, 20-min, 40-min and 60-min after the light-adapted (A) retina was left in the darkness. Scale bars indicate 50 μm.

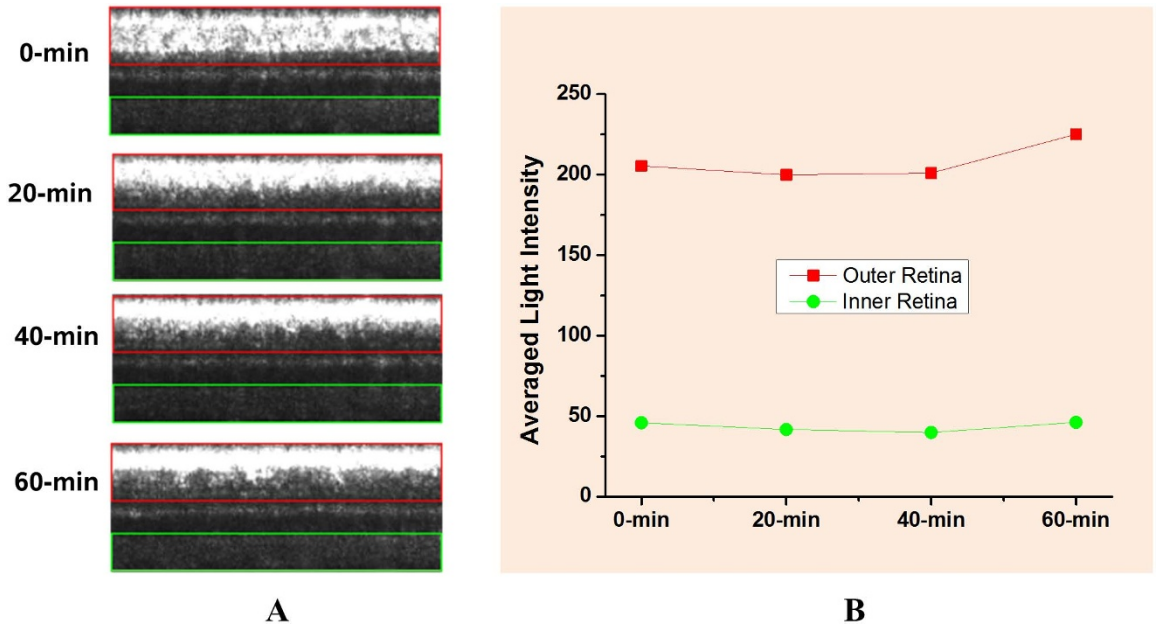

Figure 5 | Light reflectivity change of inner and outer retina during light-to-dark transition. (A) Red box indicates outer retina area with RPE complex included and green box indicates inner retina area; (B) the averaged reflectivity change of inner and outer retina during light-to-dark transition.

melanosome translocation. In order to verify it, histological examination of 0.75 μm-thick eyecup slices was conducted, with improved microscopy resolution (60×). The melanosome redistribution was clearly revealed in dark- (Fig. 6C) and light-adapted (Fig. 6D) eyes. Using 6,000× transmission electron microscopy, the structure of individual melanosomes within RPE microvilli was confirmed (inserted panel in Fig. 6D).

Discussion

In summary, we employed a custom-designed SD-OCT to achieve in vivo imaging at subcellular resolution. Comparative OCT examination of dark- and light-adapted frog eyes verified that RPE melanosomes are a primary source of reflectivity. Early polarization-sensitive OCT imaging has suggested that RPE OCT signal could be attributed to RPE melanosomes[24–27]. Melanosome is an organelle that synthesizes and stores melanin. In humans, the melanin determines the skin color. Besides in the RPE, It is also found in hair, the pigmented tissue underlying the iris of the eye and the brain. Melanin has a high index of refraction[28,29], in confocal microscopy images, and thus melanin has been shown to provide strong contrast[30]. OCT images of brain, skin and hair also indicate higher scatter or increased signal in melanin accumulated area[28,29,31–33].

The purpose of this study is to use the unique animal (frog) model, which possesses light-driven melanosome translocation, to test the OCT correlate (i.e. melanosomes) in retinal RPE. Our experiment results showed OCT imaging consistently revealed a hyper-reflective band at the RPE in dark-adapted retinas, which was much stronger than other hyper-reflective bands such as the ELM and photoreceptor ISe. Given the fact that melanosomes were aggregated at the apical aspect of the RPE in dark-adapted eyes (Fig. 1, left, Fig. 5A and 5C), the observed hyper-reflective OCT band observed at the RPE (Fig. 2A–B) supported the primary scatter candidacy of melanosomes on OCT imaging. When the frog eye was exposed to visible light illumination, reflectivity of the RPE band was decreased gradually. In contrast, the reflectivity of photoreceptor band, particularly the inner segment, was enhanced, and the ELM band merged with the photoreceptor ISs band (Fig. 4A–B). This phenomenon was consistent with the histological observation in light- adapted retina, in which RPE melanosome translocated within the apical processes from proximal to distal (up to the ELM) (Fig. 6B and 6D). In other words, our observed OCT dynamics associated with light changes tightly correlated with RPE melanosome redistribution shown in Fig. 1. In-depth understanding of the OCT correlates in the outer retina will pave the way for quantitative analysis of OCT outcomes.

Although light-driven melanosome translocation has not been consistently observed in human and mammal animals[34], recent study has suggested possible changes of RPE melanosomes correlated with light/dark adaptation in human eye. Moreover, RPE abnormality is a common occurrence associated with AMD[7,8], and RPE pigment relocation has been reported in mouse models of inherited retinopathies[28] and human patients with retinitis pigmentosa[29] and AMD[30]. In *vivo* ophthalmologic imaging of retinal and corneal morphology with an axial resolution of 1–2 μm was present for human eye imaging. Therefore, we expect that the pathological translocation of RPE melanosomes in human subjects can be quantitatively assessed by the OCT. In addition, in vivo functional OCT imaging may advance the study of RPE/photoreceptor interactions in animal models. Without the requirement of destructive histologic preparations[21], OCT imaging of the RPE/photoreceptor dynamics is easy, time- and cost-effective. Besides, functional OCT imaging of the same animals under different light conditions can be reliably implemented, without artifacts due to different samples prepared for endpoint histologic examination. Previous studies have suggested that melanosome aggregation towards the dark-adapted position could depend upon the external ionic concentration, such as the external Ca^{+2} or Na^{+} [21], as well as the elevated intracellular cAMP[35]; while melanosome dispersion to the light-adapted position was affected by chemical messengers such as dopamine[21,35] rather than the Ca^{+2} or Na^{+} concentration. It can provide excellent models to investigate the diurnal and circadian regulation of photoreceptor and RPE physiology[36]. For example, the recognition of the role that dopamine plays in light and circadian signaling. The demonstrated *in vivo* OCT imaging will allow quantitative analysis of effects of these physiological parameters by longitudinal monitoring of animal retinas under variable pharmacological treatments.

Methods

Animal preparation. Adult northern leopard frogs (Rana Pipiens) were used in this study. The experimental procedure was approved by the Institutional Animal Care and Use Committee of the University of Alabama at Birmingham and carried out in

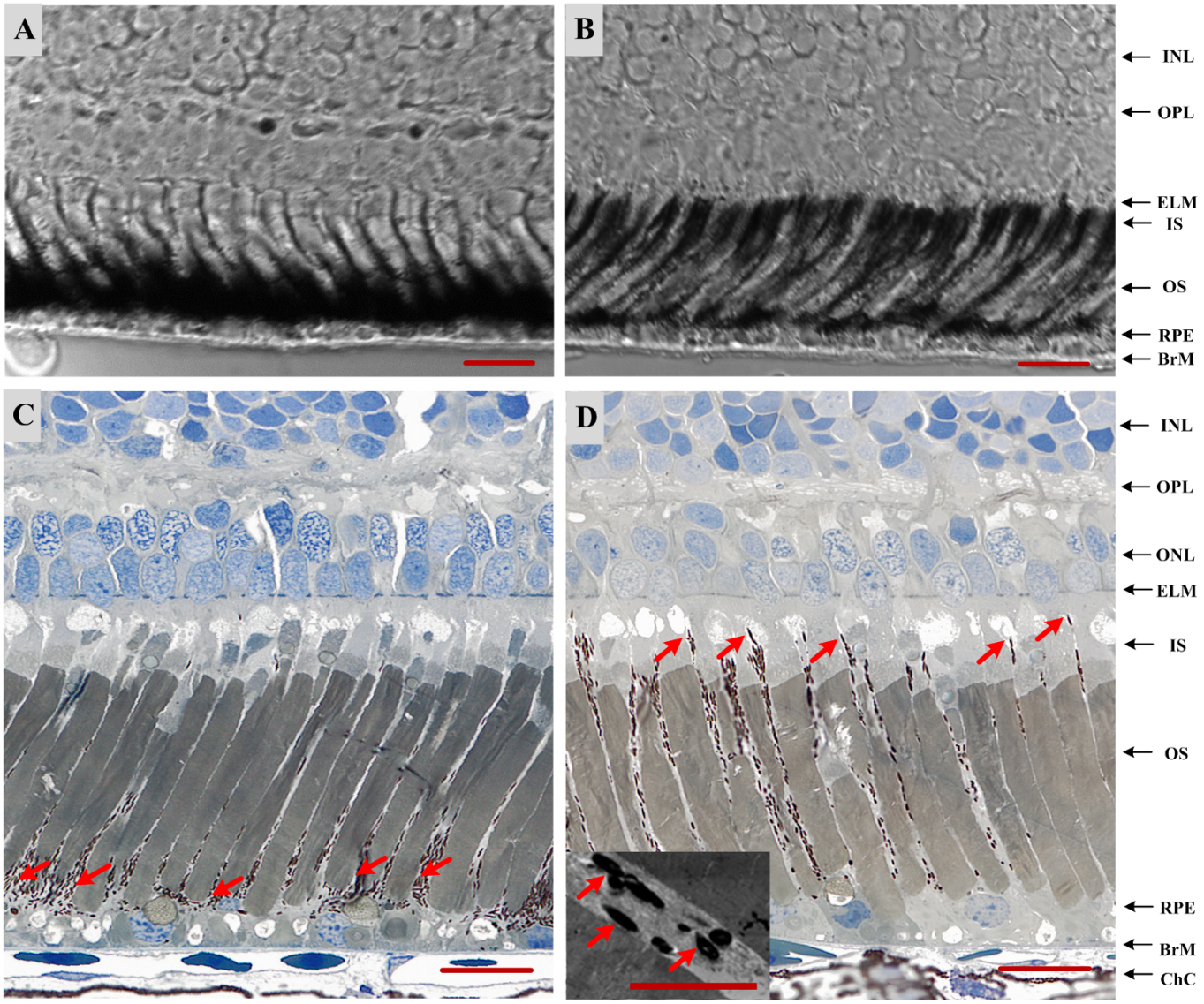

Figure 6 | Histological images of dark- (A, C) and light-adapted (B, D) frog eyes. For (A) and (B), images unstained 14 μm thick frozen sections were obtained by bright field microscopy (40×) with N.A. 0.95 objective; For (C) and (D), section thickness is 0.75 μm, and images were obtained by bright field microscopy (60×) with N.A. 1.4 objective. The inset to panel (D) shows individual melanosomes (arrows) within apical processes of RPE, flanked by photoreceptor outer segments, as obtained by transmission electron microscopy (6000× original magnification). Scale bars indicate 25 μm in (A–D) and 5 μm for (D) inset.

accordance with the guidelines of the ARVO Statement for the Use of Animals in Ophthalmic and Vision Research.

In vitro histological preparation. Following over-night dark adaptation and 8-hour light adaptation, frogs were euthanized by rapid decapitation and double pithing before enucleating the eyes. After the eyes were removed from the sockets, 1–2 small holes were created by a needle at the cornea of the intact eyes, and the eyeballs were still spherical in shape. Then eyes were immersed in 4% paraformaldehyde for 3 hours and hemisected below the equator with a pair of fine scissors to remove the lens and anterior structures. After that, the complete retina-RPE-choroid-sclera complexes were transferred to 2% paraformaldehyde and 0.25% glutaraldehyde for storage. For dark-adapted frogs, procedures were conducted in a dark room with dim red illumination. After fixation, retinas were cryoprotected in 30% sucrose, embedded in a 2/1 mixture of 30% sucrose and frozen tissue embedding media (HistoPrep; FisherScientific, Pittsburg, PA) and cryo-sectioned (14 μm sections), thaw-mounted on SuperFrost plus slides (Fisher Scientific, Pittsburg, PA) and stored at 2°C until use. Images were obtained using a Zeiss Axioplan2 microscope, a 40× objective with numerical aperture = 0.95. Another set of eyes was post-fixed in osmium tannic acid paraphenylenediamine, dehydrated with ethanol and acetonitrile for semi-thin (0.75 μm) epoxy sections in the horizontal plane through the optic nerve[37]. Images were obtained using bright field microscopy, a 60× oil objective with numerical aperture = 1.4, and a CCD camera (Olympus XC10). High resolution (6,000×) transmission electron microscopy was also conducted to confirm the structure of individual melanosomes.

In vivo SD-OCT imaging. To compare the melanosome position differences under light and dark conditions, frogs underwent the over-night dark adaptation and 8-hour light adaptation, respectively. Before NIR (Near Infrared) OCT imaging, the frog was anesthetized through the skin when it was immersed in the tricaine methanesulfonate (TMS, MS-222) solution (500 mg/liter)[38]. After confirmation of the anesthesia, topical atropine (0.5%) and phenylephrine (2.5%) were applied to fully dilate the pupil to ~5 mm. After that, the frog was placed in a custom-built holder for OCT imaging. The holder provided six degrees of freedom to facilitate adjustment of body orientation and retinal area for OCT imaging[39].

For the experiment designed to monitor melanosome movement from light to dark, after the initial 8-hour light adaptation, the frog eyes were imaged under light condition for the first half hour at 10 min intervals. Then the eyes would be left in full darkness. The 10 min intervals NIR retinal imaging was performed continuously for another one hour in the dark. In order to optimize the comparison between light and darkness, we imaged the identical areas in the retina over time.

SD-OCT system configuration. A schematic diagram of our SD-OCT system is illustrated in Fig. 7. The light source used in this system is a broadband superluminescent diode (SLD; Superlum Ltd., Ireland) with a center wavelength of

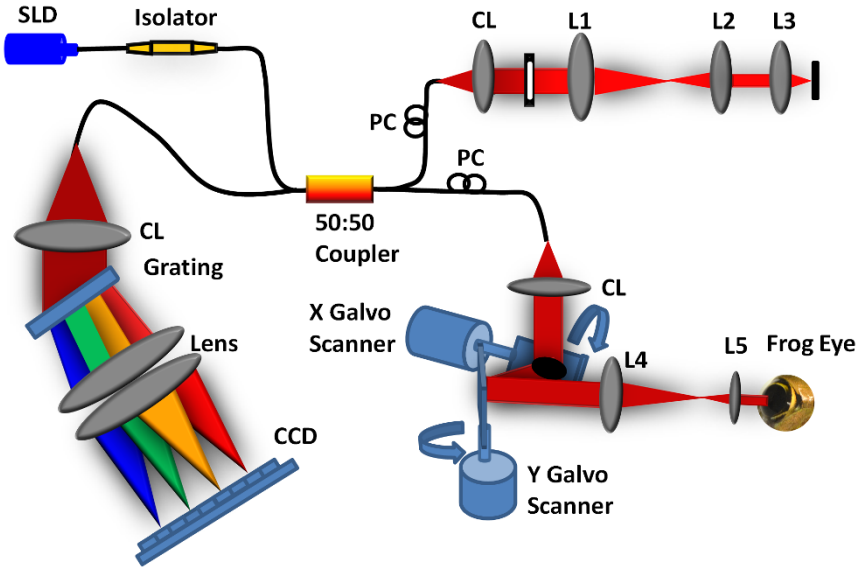

Figure 7 | Schematic diagram of the experimental setup. Schematic of the SD-OCT system at 846 nm designed to acquire *in vivo* images of the retina of the frog eye. SLD: superluminescent diode, PC: polarization controller, CL: collimation lens, L1–L5: lens. Focal lengths of lenses L1, L2, L3, L4, and L5 are 75, 50, 15, 100, and 30 mm, respectively. The photograph of the frog eye was taken by Qiu-Xiang Zhang.

846 nm, full width at half maximum (FWHM, $\Delta\lambda$) of 104 nm. The beam from the SLD is coupled to fiber-based Michelson interferometer via a 50 : 50 fiber coupler (Thorlabs, Inc., USA), which split the source light into the sample and the reference arms. A fiber optic isolator (Thorlabs, Inc., USA) is employed between the SLD and the fiber coupler to exclude back reflection. The sample arm consists of an X-Y transverse galvanometer scanner and a pair of relay lens for delivering sample light to the frog retina and collecting the back-reflected sample light. The optical power entering the pupil which meets the safety requirements set by the American National Standards Institute (ANSI) Z136.1 limits. In the reference arm, we employed similar lenses to match the dispersion between the reference and the sample arms. Instead of a neutral density filter, a slit was used to adjust reference power without inducing extra dispersion.

The interference signal between the reference arm and sample arm was collected by the fiber coupler and delivered to a custom-built spectrometer. The spectrometer consists of an IR achromatic f = 150 mm doublet lens (Thorlabs, Inc., USA) as the collimator, a 1200 line/mm transmission grating (Wasatch Photonics, Inc., USA) and rapid rectilinear lenses with two 300 mm achromatic doublet lens pair (Thorlabs, Inc., USA). The detector is a line scan charge-coupled device camera (EV71YEM4CL2014-BA9 OCT/Spectrometer versions, E2V, NY, USA) with 2048 pixels and 14 μm × 28 μm pixel sizes. The calculated spectral resolution was 0.0498 nm, which corresponds to a detectable depth range of 3.59 mm in air[40].

An image acquisition board acquired the image captured by the camera and transferred it to a computer workstation (Intel Xeon CUP, dual 2.26 GHz processor, 6 GB memory; Dell Inc., Texas, USA) for signal processing and image display. The A-line (depth scan) rate of the OCT system was set at 5 kHz. At this operating condition, the OCT sensitivity was approximately 95 dB. The numerical aperture of the system is 0.4 with depth of focus around 6 μm. The theoretical axial resolution was approximately 3.04 μm in air, corresponding to 2.25 μm in tissues[40] (the refractive index of the retina was approximately 1.35) and theoretical lateral resolution around 2 μm.

1. Strauss, O. The retinal pigment epithelium in visual function. *Physiological reviews* **85**, 845–881 (2005).
2. Bok, D. The retinal pigment epithelium: a versatile partner in vision. *Journal of cell science. Supplement* **17**, 189–195 (1993).
3. Kevany, B. M. & Palczewski, K. Phagocytosis of retinal rod and cone photoreceptors. *Physiology* **25**, 8–15 (2010).
4. Bok, D. Retinal photoreceptor-pigment epithelium interactions. Friedenwald lecture. *Invest Ophthalmol Vis Sci* **26**, 1659–1694 (1985).
5. Bok, D. Processing and transport of retinoids by the retinal pigment epithelium. *Eye* **4**, 326–332 (1990).
6. Sarna, T. Properties and function of the ocular melanin--a photobiophysical view. *Journal of photochemistry and photobiology. B, Biology* **12**, 215–258 (1992).
7. Bhutto, I. & Lutty, G. Understanding age-related macular degeneration (AMD): relationships between the photoreceptor/retinal pigment epithelium/Bruch's membrane/choriocapillaris complex. *Molecular aspects of medicine* **33**, 295–317 (2012).
8. Panthier, C., Querques, G., Zerbib, J. & Souied, E. H. Spontaneous combined full-thickness retinal and pigment epithelium macular hole in age-related macular degeneration. *Ophthalmic surgery, lasers & imaging retina* **44**, 208–210 (2013).
9. Congdon, N. *et al.* Causes and prevalence of visual impairment among adults in the United States. *Arch Ophthalmol* **122**, 477–485 (2004).
10. Resnikoff, S. *et al.* Global data on visual impairment in the year 2002. *Bulletin of the World Health Organization* **82**, 844–851 (2004).
11. Friedman, D. S. *et al.* Prevalence of age-related macular degeneration in the United States. *Arch Ophthalmol* **122**, 564–572 (2004).
12. Drexler, W. *et al.* Ultrahigh-resolution ophthalmic optical coherence tomography. *Nature medicine* **7**, 502–507 (2001).
13. Hood, D. C. *et al.* The inner segment/outer segment border seen on optical coherence tomography is less intense in patients with diminished cone function. *Investigative ophthalmology & visual science* **52**, 9703–9709 (2011).
14. Huang, D. *et al.* Optical coherence tomography. *Science* **254**, 1178–1181 (1991).
15. Wojtkowski, M., Leitgeb, R., Kowalczyk, A., Bajraszewski, T. & Fercher, A. F. In vivo human retinal imaging by Fourier domain optical coherence tomography. *J Biomed Opt* **7**, 457–463 (2002).
16. Srinivasan, V. J. *et al.* Noninvasive volumetric imaging and morphometry of the rodent retina with high-speed, ultrahigh-resolution optical coherence tomography. *Investigative ophthalmology & visual science* **47**, 5522–5528 (2006).
17. Konno, S., Akiba, J. & Yoshida, A. Retinal thickness measurements with optical coherence tomography and the scanning retinal thickness analyzer. *Retina* **21**, 57–61 (2001).
18. Koozekanani, D., Boyer, K. & Roberts, C. Retinal thickness measurements from optical coherence tomography using a Markov boundary model. *IEEE transactions on medical imaging* **20**, 900–916 (2001).
19. Spaide, R. F. & Curcio, C. A. Anatomical correlates to the bands seen in the outer retina by optical coherence tomography: literature review and model. *Retina* **31**, 1609–1619 (2011).
20. Spaide, R. F. Questioning optical coherence tomography. *Ophthalmology* **119**, 2203–2204 e2201 (2012).
21. Mondragon, R. & Frixione, E. Retinomotor movements in the frog retinal pigment epithelium: dependence of pigment migration on Na+ and Ca2+. *Experimental eye research* **48**, 589–603 (1989).
22. Burnside, B., Adler, R. & O'Connor, P. Retinomotor pigment migration in the teleost retinal pigment epithelium. I. Roles for actin and microtubules in pigment granule transport and cone movement. *Investigative ophthalmology & visual science* **24**, 1–15 (1983).
23. Lythgoe, J. N. & Shand, J. Endogenous circadian retinomotor movements in the neon tetra (Paracheirodon innesi). *Investigative ophthalmology & visual science* **24**, 1203–1210 (1983).
24. Ahlers, C. *et al.* Imaging of the retinal pigment epithelium in age-related macular degeneration using polarization-sensitive optical coherence tomography. *Invest Ophthalmol Vis Sci* **51**, 2149–2157 (2010).
25. Baumann, B. *et al.* Polarization sensitive optical coherence tomography of melanin provides intrinsic contrast based on depolarization. *Biomedical optics express* **3**, 1670–1683 (2012).
26. Cense, B. *et al.* Retinal imaging with polarization-sensitive optical coherence tomography and adaptive optics. *Optics express* **17**, 21634–21651 (2009).

27. Gotzinger, E. *et al*. Retinal pigment epithelium segmentation by polarization sensitive optical coherence tomography. *Optics express* **16**, 16410–16422 (2008).
28. Barton, J. K. *et al*. Investigating sun-damaged skin and actinic keratosis with optical coherence tomography: a pilot study. *Technology in cancer research & treatment* **2**, 525–535 (2003).
29. Wang, X. J. *et al*. Characterization of human scalp hairs by optical low-coherence reflectometry. *Opt Lett* **20**, 524–526 (1995).
30. Rajadhyaksha, M., Grossman, M., Esterowitz, D., Webb, R. H. & Anderson, R. R. In vivo confocal scanning laser microscopy of human skin: melanin provides strong contrast. *The Journal of investigative dermatology* **104**, 946–952 (1995).
31. Boppart, S. A., Brezinski, M. E., Pitris, C. & Fujimoto, J. G. Optical coherence tomography for neurosurgical imaging of human intracortical melanoma. *Neurosurgery* **43**, 834–841 (1998).
32. Korde, V. R. *et al*. Using optical coherence tomography to evaluate skin sun damage and precancer. *Lasers in surgery and medicine* **39**, 687–695 (2007).
33. Choi, W. J., Pi, L. Q., Min, G., Lee, W. S. & Lee, B. H. Qualitative investigation of fresh human scalp hair with full-field optical coherence tomography. *J Biomed Opt* **17**, 036010 (2012).
34. Abramoff, M. D. *et al*. Human photoreceptor outer segments shorten during light adaptation. *Invest Ophthalmol Vis Sci* **54**, 3721–3728 (2013).
35. Burnside, B. Light and circadian regulation of retinomotor movement. *Progress in brain research* **131**, 477–485 (2001).
36. Menger, G. J., Koke, J. R. & Cahill, G. M. Diurnal and circadian retinomotor movements in zebrafish. *Visual Neurosci* **22**, 203–209 (2005).
37. Curcio, C. A. *et al*. Human chorioretinal layer thicknesses measured in macula-wide, high-resolution histologic sections. *Investigative ophthalmology & visual science* **52**, 3943–3954 (2011).
38. Cakir, Y. & Strauch, S. M. Tricaine (MS-222) is a safe anesthetic compound compared to benzocaine and pentobarbital to induce anesthesia in leopard frogs (Rana pipiens). *Pharmacological reports: PR* **57**, 467–474 (2005).
39. Zhang, Q. X., Lu, R. W., Curcio, C. A. & Yao, X. C. In vivo confocal intrinsic optical signal identification of localized retinal dysfunction. *Investigative ophthalmology & visual science* **53**, 8139–8145 (2012).
40. Wojtkowski, M. *et al*. Ultrahigh-resolution, high-speed, Fourier domain optical coherence tomography and methods for dispersion compensation. *Optics express* **12**, 2404–2422 (2004).

Acknowledgements

The authors wish to thank Dr. Shuliang Jiao for his valuable advice on OCT construction, and thank Cham K. Yao for preparing the cartoon illustration in Fig. 1. Q.X.Z., R.W.L. and X.C.Y. are supported by NSF CBET-1055889, NIH R21 EB012264, and UASOM I3 Pilot Award. CAC and JDM are supported by NIH R01 EY06109 and institutional support from the Eyesight Foundation of Alabama and Research to Prevent Blindness, Inc. V.G. is supported by Vision Sciences Core grant NIH P30 EY03039.

Author contributions

Q.X.Z. contributed to OCT construction, performed OCT imaging and data processing, and contributed to manuscript preparation. R.W.L. contributed to optical construction and data processing. J.D.M. and V.G. performed histological examination. C.A.C. contributed to histological examination, experimental design, and manuscript preparation. X.C.Y. conceived and supervised the project, contributed to OCT design, experimental design, data analysis and manuscript preparation.

Additional information

Competing financial interests: The authors declare no competing financial interests.

How to cite this article: Zhang, Q. *et al. In vivo* Optical Coherence Tomography of Light-Driven Melanosome Translocation in Retinal Pigment Epithelium. *Sci. Rep.* **3**, 2644; DOI:10.1038/srep02644 (2013).